# Accepted Manuscript

Title: Tilting separation analysis of bottom-up mask projection stereolithography based on cohesive zone model

Author: Xiangquan Wu Qin Lian Dichen Li Zhongmin Jin

Please cite this article as: Wu, Xiangquan, Lian, Qin, Li, Dichen, Jin, Zhongmin, Tilting separation analysis of bottom-up mask projection stereolithography based on cohesive zone model.Journal of Materials Processing Technology http://dx.doi.org/10.1016/j.jmatprotec.2016.12.016

Tilting separation analysis of bottom-up mask projection stereolithography based on cohesive zone model

Xiangquan Wu[a], Qin Lian[a]*, Dichen Li[a], Zhongmin Jin[abc]

[a]State Key Laboratory for Manufacturing Systems Engineering, Xi'an Jiaotong University, 710054, Xi'an, Shaanxi, China
[b]School of Mechanical Engineering, Southwest Jiaotong University, Chengdu, Sichuan, China
[c]Institute of Medical and Biological Engineering, School of Mechanical Engineering, University of Leeds, Leeds LS2 9JT, UK

*Corresponding author: Qin Lian
E-mail address: lqiamt@mail.xjtu.edu.cn

**Abstract**

Compared with top-down stereolithography, bottom-up mask projection stereolithography can reduce the start filling volume of vat and is able to build components with high-viscosity materials. For general photosensitive materials, a separation process is required to detach the cured layer from the resin vat surface in order to accomplish the fabrication of current layer. The separation process can be achieved without damaging the part by utilizing appropriate platform motions including pulling-up, tilting and shearing, and covering inert film on the vat surface. The tilting separation is used in both industrial and academic area. However, there is a limited corresponding study compared with pulling-up separation. The mechanism of tilting separation and its effects on separation force and fabrication process are not clear. In this paper, an analytical model based on cohesive zone model was formed and a specialized experimental system was built. Experimental studies on the tilting effects on cohesive stiffness and fracture energy were conducted by collecting and analyzing separation force data. The results showed that changing exposure area function or the part fabrication orientation changed the cohesive stiffness, and increasing tilting separation velocity caused different increase in fracture energy when using different inert films. The results of this investigation can be used to choose the reasonable platform motion and process parameters by considering the part geometry and the characteristics of both inert film and materials.

**Keywords:** Additive manufacturing; Bottom-up mask projection stereolithography; Tilting separation; Cohesive zone model; Pulling-up separation; Separation force

## 1. Introduction

Stereolithography is the first additive manufacturing (AM) technology that utilizes photopolymerization process to fabricate three dimensional objects. The scanning laser is used to cure photosensitive resin in a vat line by line and achieves high dimensional accuracy of part (Hull, 1986). Instead of using laser, mask projection stereolithography (MPSL) uses a pattern generator such as digital mirror device (DMD) to dynamically generate mask to cure a whole layer once (Choi et al., 2009) or generate masks to cure a layer in a scanning manner (Emami et al., 2015).

The bottom-up MPSL creates a constrained liquid layer between previously cured part and the vat surface before each curing procedure. The constrained liquid layer is then selectively cured according to the mask shape during curing procedure. Compared with top-down stereolithography, several advantages can be obtained by applying bottom-up MPSL (Fig. 1). The vertical direction curling of cured part that occurs in top-down stereolithography (Xu and Chen, 2014) can be reduced since the photopolymerization of bottom-up MPSL is reacted in a constrained area (Huang and Lan, 2006). The part fabrication with high-viscosity (Felzmann et al., 2012) materials is achieved because the recoating step (Renap and Kruth, 1995) is simplified. Only small amount of material is needed to start the fabrication since there is no need to maintain a whole tank of material (Zhou et al., 2013).

The curing process leads to adhesion at two interfaces of the constrained layer, as shown in Fig. 2 (a). In order to proceed the whole fabrication process, the cured layer should be separated from the vat surface. Therefore, the force needed to separate the lower interface should be smaller than the force needed of the upper interface; otherwise, the part will be broken, as show in Fig. 2 (b). During the whole process of part fabrication, it is necessary to ensure that each separation is successfully accomplished, which becomes a unique problem of bottom-up MPSL.

Different motions of the platform can be used to achieve separation, including pulling-up, tilting and shearing (Fig. 3). Most of industrial bottom-up MPSL machines use pulling-up as the separation method. The Prefatory of EnvisionTEC Company is the first industrial bottom-up MPSL machine using digital light processing (DLP) technology of Texas Instruments, and the company uses tilting mechanism to assist separation process (John, 2007). Pan et al. (2012b) developed a two-channel system wherein the vat surface was half coated with polydimethylsiloxane (PDMS). After curing a layer, the vat moved in x-y plane so that the adhesion was broken by shear force, and this method was also used in B9creator MPSL machine (Joyce, 2012). The Cerafab from Lithoz GmbH (Schwentenwein and Homa, 2015), which was designed for manufacturing high performance ceramics, applied tilting mechanism as one optional process procedure of ceramic green body fabrication (Felzmann et al., 2012).

Inert films such as fluorinated ethylene propylene (FEP), polytetrafluoroethylene (PTFE) and PDMS are used to reduce the separation force. Tumbleston et al. (2015) demonstrated a method which created an oxygen inhibited liquid interface in the exposure area of bottom-up MPSL. This method avoided the generation of separation force for free-radical system resin that has oxygen

inhibition and realized fast continuous printing. However, this method still has problems for fabrication parts with large section area and materials of other system or high viscosity materials like ceramic slurry. The inert film method is a common practice of bottom-up MPSL because its high adaptability. However, the inert film cannot avoid separation force completely. The adhesion between film and cured photopolymer forms during each layer fabrication.

The separation in bottom-up MPSL is a fracture behavior between different materials. After each layer curing, the inert film and the cured layer form a laminated composite structure. So the method for failure analysis of laminated composite structure can also be used to analyze the separation in bottom-up MPSL, such as virtual crack closure technique (VCCT) and cohesive zone model (CZM). VCCT was first proposed by Rybicki and Kanninen (1977) and it was based on the linear-elastic fracture mechanics. However, VCCT cannot simulate crack initiation and it is only available in highly specialized finite element software (Ye et al., 2015). CZM is another model used for delamination simulation. Barenblatt (1962) first proposed this kind of model and referred the opening crack zone as cohesive zone. CZM is a physically motivated model that assumes the

fracture only occurs in a narrow strip zone(Kuna, 2013). A certain distance $\delta^f$ is used for

dividing the narrow strip zone into stress free area and cohesive zone, as shown in Fig. 4. The stress free area means the new surfaces after crack are generated. The traction stress T is used to describe the stress state in the cohesive zone. $T^0$ is the maximum traction stress and is also called the cohesive strength. Cohesive zone is not the true adhesion zone of laminated composite structure, but it gives a general discerption of the crack initiation and the crack propagation of existing cracks.

In order to investigate the mechanism of separation force, Liravi et al. (2015) characterized the pulling-up separation in terms of CZM, and built a finite element model using Abaqus software to simulate the deformation of the PDMS film. Ye et al. (2015) conducted both experimental tests and numerical simulation to study the effects of pulling-up velocity on separation force, and found CZM was eligible for simulating separation force under different pulling-up velocities. Huang and Jiang (2005) developed a separation force monitoring system for bottom-up MPSL, and used the crack initiation toughness $\sigma_{IC}$ as one constituent of separation force based on experimental results. Zhou et al. (2013) conducted a series of experiments to investigate the relationship of mask shape, exposure time and mask area with separation force.

However, the research mentioned above mainly studied the effects of pulling-up separation without considering the tilting separation, which is used in industrial and academic designs of bottom-up MPSL. There is no analytical model that describes the tilting separation mechanism and it is hard to choose the separation method under a given condition or a given material due to the lack of tilting separation force data. The effects of tilting on separation force and fabrication process are unclear and the industrial bottom-up MPSL machines with tilting is not capable of conducting experiments with designed parameters.

To understand the mechanism and effects of tilting separation, this investigation established an analytical model of tilting separation based on CZM and built a specialized experimental system with tilting function. Three experiments were designed for verifying the analytical model. A force sensor was used to collect separation force data. Tilting effects on cohesive stiffness and fracture

energy were focused to compare with pulling-up. Tilting cohesive stiffness and tilting fracture energy were quantified. The stress distribution at the exposure area was analyzed through a test sample fabrication. The effects of tilting on fabrication process were discussed.

## 2. Analytical model of tilting separation
### 2.1 Bilinear cohesive law

The function that describes the separation force plays a central role in CZM, and it is also called the cohesive law or cohesive curve. This law is a relationship between separation distance $\delta$ and traction stress $T$. There are several effective cohesive laws such as cubic polynomial, trapezoidal, exponential, bilinear etc. (Park and Paulino, 2011). The bilinear law was used in studies of pulling-up separation and is proved eligible for simulating the stress and strain distribution of the inert film (Liravi et al., 2015). In this present paper, the bilinear law of CZM was chosen to establish the analytical model of tilting separation.

The Mixed-mode of bilinear cohesive law (Camanho et al., 2003) is illustrated in a three-dimensional map as shown in Fig. 5. Mode I cohesive law, which describes the separation force caused by the perpendicular movement between two crack faces, is represented in $0\text{-}T\text{-}\delta_n$ plane. Mode II cohesive law, which describes the separation force caused by the tangential movement, is represented in $0\text{-}T\text{-}\delta_t$ plane. The pulling-up separation can be classified as mode I because the cured part moves vertically to the vat surface during the separation. $\delta_n$ is the normal separation distance and $\delta_t$ is the tangential separation distance. Any point in $0\text{-}\delta_n\text{-}\delta_t$ plane represents a displacement of mixed-mode. The traction stress reaches the highest value $T^0$ when the separation distance equals to $\delta^0$ and it is the crack initiation point. Integrating the cohesive law from 0 to $\delta^f$ yields the area under the curve, which is equal to the fracture energy $G$. $K$ represents the slope of bilinear cohesive law before $\delta^0$ and it is called the cohesive stiffness. $K_n$, $K_t$ are the cohesive stiffness of mode I, II respectively.

### 2.2 Analytical model establishment

The crack opening of tilting separation has normal and tangential movements as shown in Fig. 6. The x-y plane represents the vat surface and the rotation angle $\theta$ around y axis represents the tilting angle. $P_i$ represents different points of the exposure area along x axis. The actual $\delta^f$ was smaller than 400um (Zhou et al., 2013) when using photosensitive resin as material and PDMS as inert film, so it is assumed that $\theta$ is a small angle according to the dimension of the tilting mechanism when $\delta^f$ is reached.

When $\theta$ is a small quantity, $\delta_n$ can be simplified as:

$$\delta_n = x\tan\theta \approx x\theta \tag{1}$$

$\delta_t$ is given by:

$$\delta_t = \delta_n \tan\theta \approx \delta_n\theta = x\theta^2 \tag{2}$$

Compared with $\delta_n$, $\delta_t$ is a high order term of $\theta$, so the tilting separation process is characterized as mode Ⅰ rather than mixed-mode. For crack opening mode Ⅰ, $K_t$ is equal to zero.

When using tilting separation, it is assumed that the separation of each small area at the exposure area fits the bilinear cohesive curve of pulling-up separation. The bilinear cohesive curve of tilting separation can be seen as the sum of bilinear cohesive curves of pulling-up separation of all small areas. The traction stress of a small area around $P_i$ before crack initiation point is given by:

$$T_{n p_i}(x,t) = K_{n p}\delta_{n p_i} = x_{p_i}K_{n p}\theta(t) \tag{3}$$

Where $T_{n p_i}$ and $\delta_{n p_i}$ represent the pulling-up traction stress and separation distance of the small

area around $P_i$ respectively, and $K_{n p}$ is the pulling-up cohesive stiffness which is independent on

different velocities. $\theta(t)$ changes with respect to different tilting velocity. The traction stress is given as follows at a given time:

$$T_{n p_i} = \theta x_{p_i}K_{n p} \tag{4}$$

It can be seen that different $T_{n p_i}$ is caused by different x positions of $P_i$, and this is shown in

three dimensional coordinate system of $\delta_{n p}$ - $T_{n p}$ -x in Fig. 7.

Integrating the traction stress over the exposure area yields the separation force at the given time:

$$F_{nt} = \int_A T_{n p}(x)dA = \int_A \theta x K_{n p}dA = K_{nt}\delta_{nt} \tag{5}$$

Where $F_{nt}$ is the tilting separation force before the crack initiation point of tilting cohesive curve, and $K_{nt}$, $\delta_{nt}$ represent the equivalent tilting cohesive stiffness and separation distance.

One of the major differences between tilting and pulling-up separation is velocity distribution along x axis at the exposure area. For each small area, the traction stress increases linearly along x axis and is also proportional to tilting angle according to equation (3). This means that tilting separation has different traction stress distribution along x axis at the exposure area compared with pulling-up separation. From equation (5), it can be concluded that $K_{nt}$ is different when the exposure area $A(x, y)$ is different function of x. The fracture energy $G_{nt}$ of tilting separation is given by:

$$G_{nt} = \int_0^{\delta_{nt}^f} T_{nt}(\delta_{nt})d\delta_{nt} \tag{6}$$

The fracture energy $G_{np}$ of pulling-up separation can be obtained in the same way. In most cases

$G_n$ is seen as a constant depending on material characteristic, however, Ye et al.(2015) observed

that in pulling-up separation $G_{n p}$ increased when increasing the separation velocity. This

rate-dependent phenomena was caused by the energy dissipation of the interface which was formed by cured resin and PDMS film (Ye et al., 2015). Due to the analytical model of tilting separation, it can be inferred that tilting separation also has the rate-dependent phenomena.

## 3. Experiments
### 3.1 Experimental setup

To verify the conclusions drawn from the analytical model, three experiments were designed and conducted using a specialized bottom-up MPSL system.

The schematic of the bottom-up MPSL system for investigating tilting separation is demonstrated in Fig. 8. The system was divided into four main modules including projection module, motion module, separation force processing module and control module. The tasks of control module were generating the mask list and synchronizing projection module with motion module. A Pro-4500 device consisting of a 0.45-inch DMD chip, a 405 nm UV-LED and a set of imaging lens were served as the projection module. The masks could be projected to the bottom of the vat according to the predefined parameters such as exposure duration and exposure intensity. An eccentric cam with oscillating roller follower mechanism was designed to meet the experimental requirements. The follower constituted the lower platform, which could oscillate around a hinge when the eccentric cam rotated. The resin vat was fixed on the lower platform surface. In order to change the inert film for different experiment groups, two resin vats with different films glued to their surfaces were used. The upper platform could only move along Z direction. A square glass (thickness: 4mm, area: $687.5mm^2$) are glued to the bottom center of the upper platform as shown in Fig. 2(b) to which the fabricated part is attached. In order to precisely control and monitor the motion of the upper platform, a raster ruler was installed along Z axis. The position data of the upper platform provided by the raster ruler was used in a position compensation algorithm to ensure the accuracy of the given layer thickness.

The separation force processing module was used to collecting and processing force data during separation. A calibrated LH-S05 force sensor was mounted between upper platform and Z axis moving part in order to generate the voltage signal of separation force. A voltage signal amplifier was connected to the sensor to amplify the signal to the range of 0-5V. An Arduino uno board was used to process the amplified analog signal. The microcontroller of the Arduino board collected data at intervals of 10.45 ms and sent them to the serial port of the control computer. The open source software SerialChart that could visualize the data from the serial port was applied to show the separation force on time on the computer screen.

The zero position registration of bottom-up stereolithography was critical for first several layers fabrication. A mechanism of force limit and parallelism adjustment was applied to ensure the same registration of zero position when using vat with different thickness films. The adjusting thimble on the upper platform and a level gauge were used to accomplish the adjustment of parallelism between the upper platform and the vat surface. The weight of the upper platform (7.17N) was chosen as the force limit when the upper platform contacting the vat surface, and the sensor value was zero when the force limit was reached. The whole system and the detailed specifications of the setup are shown in Fig. 9 and Table 1.

A white photosensitive resin that was produced by Zhuhai CTC electronic CO., LTD was used to conduct all the experiments. The apparent viscosity of the resin was tested using a rotational digital viscometer (NDJ-5S, Benshan Instrument, Shanghai), which was 616 mPa.s at 22 degree centigrade. The tensile properties of the resin were also tested according to ISO 527-2:1993 (Plastics -- Determination of tensile properties -- Part 2: Test conditions for moulding and extrusion plastics). The tensile strength was 29.25 MPa and the elasticity modulus was 87.75 MPa. The main curing parameters used in experiments are listed in Table 2. During fabrication process, the actual layer thickness measured by the raster ruler was $0.1\pm0.005$mm.

### 3.2 The experiment of different exposure area A(x)

The experiment which compared the effect of different A(x) on $K_{nt}$ was designed to use two same area isosceles triangles with forward and backward orientations as cured masks. Half cured parts and their locations and dimensions (listed in Table 3) are shown in a three dimensional coordinate system to represent their real condition in fabrication process (Fig. 10).

Where $L_P$ denotes the height of two isosceles triangles, and $L_T$, $L_A$ denote the half base and the position of the triangles respectively. The hypotenuse functions of the isosceles triangles are stated in equation (7) and (8). $F_{nt1}$ and $F_{nt2}$, which is the theoretical tilting separation force at a given time before crack initiation, are calculated according to equation (5) and given by equation (9) and (10). The subscripts 1 and 2 denote the parameters relative to forward triangle and backward triangle respectively.

$$y_1 = -\frac{L_T}{L_P}(x - L_P - L_A) \tag{7}$$

$$y_2 = \frac{L_T}{L_P}(x - L_A) \tag{8}$$

$$F_{nt1} = \int_{L_A}^{L_A+L_P} T_{np}(x)dA_1 = 2\int_{L_A}^{L_A+L_P} x\theta K_{np} y_1 dx = \theta L_T K_{np}\frac{3L_P L_A + L_P^{\,2}}{3} = K_{nt1}\delta_{nt}A \tag{9}$$

$$F_{nt2} = \int_{L_A}^{L_A+L_P} T_{np}(x)dA_2 = 2\int_{L_A}^{L_A+L_P} x\theta K_{np} y_2 dx = \theta L_T K_{np}\frac{3L_P L_A + 2L_P^{\,2}}{3} = K_{nt2}\delta_{nt}A \tag{10}$$

Substitution of the dimensions to equation (9) and (10) yields:

$$\left.\begin{array}{l} 132.67\dfrac{\theta}{\delta_{nt}} = \dfrac{K_{nt1}}{K_{np}} \\[2mm] 139.33\dfrac{\theta}{\delta_{nt}} = \dfrac{K_{nt2}}{K_{np}} \end{array}\right\} \rightarrow K_{nt1}/K_{nt2} = 0.952 \tag{11}$$

$F_{np1}$ and $F_{np2}$, which is the theoretical pulling-up separation force at an arbitrary time before

crack initiation, are represented by equation (12) and (13).

$$F_{np1} = K_{np1}\delta_{np}A \tag{12}$$

$$F_{np2} = K_{np2}\delta_{np}A \tag{13}$$

It is also necessary to conduct experiments to verify the equation (11) and (12), in which $K_{np1}$ and

$K_{np2}$ are independent of A(x) as shown in equation (14)

$$K_{np1} / K_{np2} = 1 \tag{14}$$

In order to compare the effects of different A(x) on pulling-up and tilting, the parameters of each process should be comparable. Because the velocity of tilting separation changes linearly along x axis, the initial tilting velocity $V_t$ at the middle point $P_{(n+1)/2}$ of the tringle height (shown in Fig. 11) was set as the same with pulling-up velocity $V_p$, and all the comparative experiments between pulling-up and tilting were based on this setting. The initial tilting velocity $V_t$ of $P_{(n+1)/2}$, also called equivalent separation velocity , was calculated accord to the dimension of the oscillating roller follower mechanism and the cam profile (listed in Table 1), and controlled by the cam rotating velocity. The velocity of 0.1mm/s and FEP film were chosen as the unchanged parameters, and four separation data sets (listed in Table 4) were collected for comparison.

In the fabrication process, the filling height of the resin was 2 mm, so the square glass upper platform dipped into the resin until 20 layers fabrication. The immersion condition of the upper platform at the beginning of a fabrication process has influence on the resin flowing during separation. According to Pan Yayue (Pan et al., 2012a), the flowing of resin during separation generates force to the upper platform, which affects the measured separation force. In order to study and decrease the resin flowing effect, the separation force from the first layer fabrication was measured under the condition of exposure and no exposure. The parameters of 1-T-1 in Table 4 were used. The result of this pre-experiment was used to guide the force data collecting strategy of the experiments in this paper.

### 3.3 The experiment of different separation velocity

To investigate the effect of different separation velocity on $G_{nt}$ when using PDMS or FEP as inert film, 0.1, 0.2, 0.5, 1.0, 1.5 mm/s were chosen to be the velocity set, and the backward orientation triangle was used as the mask. The separation data sets are listed in Table 5.

In the fabrication process of normal MPSL, the separation method and velocity are the same for each layer fabrication of the part. It was observed that restart of the fabrication process caused more instability of separation force than a continuous fabrication process. In order to reduce the number of restart times, an automatic fabrication procedure was designed to conduct the two experiments described above together. In this procedure (Fig. 11), the experiment listed in Table 4 is conducted firstly and the experiment listed in Table 5 is then conducted. Since different inert films were glued to different vats, changing vat is inevitable when changing inert film. In one automatic fabrication procedure, only one kind of inert film and mask could be used, so four automatic procedures were conducted to obtain all the data sets. It should be noted that changing film and mask caused reregistration of zero position. According to the force limit mechanism of zero position registration, changing vat brought slight difference for separation force of first

several layers. For each procedure, a 1 mm thickness base was built first in order to increase the accuracy of force data according to the result of the pre-experiment (see section 4.1, Fig. 13).

### 3.4 The experiment of stress distribution at the exposure area

Since the stress distribution at the exposure area was hard to measure, in order to investigate the difference in stress distribution between tilting separation and pulling-up separation, a test sample (Fig. 12) was designed to indicate the difference. The parameters listed in Table 4 except for the mask were used in this experiment. Firstly, a 1.5mm thickness cuboid was built for constructing a solid base of the sample. Then two columns of pillars were fabricated on the base. The final layer was one column of rectangular planes. The separation force needed for separate the rectangular planes was offered by the pillars when finishing the final layer fabrication. The pillars could be broken due to the large separation force, and it also demonstrated the structure failure during fabrication. The broken section of the pillar was designed to be a 0.2×0.2 mm square that was four white pixels in the pixel-based mask. The dimensions of the pillar and the rectangular plane were selected by trial-and-error tests.

## 4. Experimental Results
### 4.1 Different exposure area A(x)

The measured force under the condition of exposure and no exposure is shown in Fig. 13. In order to show the effect of zero position registration, the weight of the upper platform is not subtracted from the force data. The cycle of the fabrication process is also described in Fig. 13.

Fig. 14 shows the separation force data in the form of cohesive curve. Two groups of 1-T-2 data set and one group of 1-T-1 date set are selected to compare their cohesive stiffness. Two groups of 1-P-1 data set and one group of 1-p-2 data set are presented in the same manner.

Fig. 15 shows the linear fit results of cohesive stiffness of all the data sets listed in Table 4, and the ratio of $K_{nt1} / K_{nt2}$ and $K_{np1} / K_{np2}$ are listed in Table 6.

### 4.2 Different separation velocity

The data set of 2-T-1 and 2-T-2 are presented in the form of cohesive curve in Fig. 16.

The maximum separation forces using different separation methods and inert films are shown in Fig. 17. The quantification results of fracture energy are shown in Fig. 18.

### 4.3 Stress distribution at the exposure area

The attached position of the rectangular planes indicates the stress distribution at the exposure area (Fig. 19). Fig. 19 (a) and (b) shows the test samples that detached from upper platform and (c) and (d) shows the unseparated rectangular planes that still attached to the vat surface. Fig. 20 demonstrates the magnified pillars.

## 5. Discussion

The cohesive curve is critical to understand the difference of separation process under various conditions. The key variables (cohesive stiffness $K$, fracture energy $G$, maximum traction stress $T^0$) of cohesive curve offer explanation of the differences between tilting and pulling-up. Experiment 1 and 2 described in section 3.2 and 3.3 are used to give quantitative comparison of the key variables for varifying the analytical model established in section 2.2.

The stress distribution can represent separation process in another way, which can not be expressed by cohesive curve. Experiment 3 described in section 3.4 is used to give a visible indication of the stress distribution of different separation methods.

### 5.1 The effect of different A(x) on the cohesive stiffness $K_{nt}$ of tilting separation

The results of the pre-experiment (Fig. 13) shows the effect of zero registration and resin flow on measured separation force. It can be observed that the force limit used in zero registration only has influence on the first three layers fabrication. After six layers fabrication, the force caused by the resin flow is less than 0.4 N (the upper platform immerses in the resin until 20 layers fabrication). Therefore, the fabrication of 1 mm thickness base before force collecting can help increase the accuracy of separation force data.

The experiment results (Fig. 14) shows that tilting separation force can be affected by the fabrication orientation of part, when changing part orientation changes the mask area distribution about x axis.

Because $A_1$ has more area in the low tilting velocity side than $A_2$, according to equation (9) and (10), the tilting separation force $F_{nt1}$ using forward triangle as mask is smaller than $F_{nt2}$ using backward triangle. As a result, the equivalent cohesive stiffness $K_{nt1}$ is smaller than $K_{nt2}$, and this can be seen from Fig. 14 (a), (b). It also can be observed that, in the descending part of the cohesive curve, which represents the separation force after crack initiation, the slopes are different either. While in the pulling-up separation process, $K_{np}$ remains unchanged when the mask orientation changes, and this phenomenon is shown in Fig. 14 (c), (d) in accordance with equation (12) and (13). The fluctuation on the curves in Fig. 14 (c), (d) is caused by the characteristic of servo motor used in Z axis, but it does not affect the trend of cohesive stiffness. Equation (11) and (14) show the theoretical ratio of $K_{nt1} / K_{nt2}$ and $K_{np1} / K_{np2}$ respectively based on the analytical model. The linear fit results of the experiment cohesive stiffness (Fig. 15 and Table 6) show the similar ratio with theoretical model. The cohesive stiffness on PDMS film is not found to have the similar ratio with theoretical model. This may due to the viscoelastic nature of PDMS (Ye et al., 2015).

### 5.2 The effect of different separation velocities on the fracture energy $G_{nt}$ of tilting separation

In experiment 2, different velocities were used to examine the change of fracture energy. The similarity that can be found between tilting and pulling-up is that both $G_{nt}$ and $G_{np}$ increase with velocity. This can be observed in cohesive curves and quantified fracture energy results (Fig. 16 (a), (b) and Fig. 18), while the increase is different between two inert films. Due to the difference in film thickness and elasticity modulus of FEP and PDMS, the fracture energy on FEP film is larger than PDMS. In terms of the magnitude of increase, $G_{nt}$ on FEP film increases 1.48 times from 0.1mm/s to 1.5mm/s, while on PDMS film it increases 3.58 times. The increase ratio for $G_{np}$ are 1.19 and 4.77 respectively. The $G_{np}$ in the present paper is at the same order of magnitude compared with the literature data (Ye et al., 2015), which used 900mm$^2$ exposure area and PDMS film.

Comparing the maximum separation force between two separation method can help us determin which method should be choosed in fabrication process. Fig. 17 shows the comparision under the condition of experiment 2. When using a higher separation velocity above 0.2mm/s, and PDMS film, tilting separation force is about 20 percent lower than pulling-up separation force.

## 5.3 The effect of tilting separation on stress distribution at the exposure area

For structure like the pillars, which carry large separation force during part fabrication, it is reasonable to decrease the local stress in the load-carrying structure area or change its position to a small stress region. The relationship (Equation 15) should be achieved to ensure defects free fabrication.

$$A_{load-carrying}\sigma_b S > T^0 A_{LSF} \tag{15}$$

Where $A_{load-carrying}$ is the area of load-carrying structure, and $A_{LSF}$ is the area of structure that caused large separation force to the load-carrying structure. $\sigma_b$ is the tensile strength of resin, and $S$ is the safe factor.

According to the analytical model presented in this paper, tilting can cause the velocity change along x axis, which will result in higher stress in high velocity side. The separated planes in Fig. 19 represent the small stress region. The number and position of these separated planes in Fig. 19 (a), (b) can indicate the different stress distribution of pulling-up and tilting. There are more separated planes near the hinge side in Fig. 19 (b), and the distribution of separated planes is more uniform in Fig. 19 (a). This indicates that tilting separation has small stress near the hinge side than the high velocity side, while the pulling-up separation has more uniform stress distribution than tilting. So it is appropriate to put the load-carrying structures area near the hinge side when using tilting. In this experiment, the uniformity of the pillars' broken section is critical. Fig. 20 shows the uniformity condition of the pillars. Since the dimensions of the pillar and the rectangular plane are selected by trial-and-error tests, the reliability and accuracy of this experiment are limited. In the future work, a more precisely predefined sample is needed and a finite element model can apply to calculate the stress distribution.

## 5.4 The effects of tilting on fabrication process

The tilting separation is achieved by tilting motion of the resin vat, which is controled by rotating the eccentric cam. This motion forces the resin to flow back and forth in the vat. The flow

can help maintain the uniformity of the material used in curing process, especially for materials easy to deposit.

The tilting can also help reduce the upper platform motion to only pull up one layer distance for each layer fabrication. However, tilting increases the complexity of the mechanism of bottom-up MPSL, and the control procedure should be changed according to the need of tilting.

## 6. Conclusion

A customized equipment with tilting function was built for the study of tilting separation force. Moreover, an analytical model of tilting separation was also developed using Mode Ⅰof crack opening and bilinear cohesive law. The bilinear cohesive curve of tilting separation is seen as the sum of pulling-up cohesive curves to which all the small areas at the exposure area conform.

Changing the function of mask area A(x) in the fabrication coordinate causes change in cohesive stiffness. The masks of forward and backward triangle with designed dimensions are used to do analytical and experimental analysis.

The linear fit results of cohesive stiffness are compared with theoretical value of analytical

model. At the velocity of 0.5mm/s, $K_{nt1}$ / $K_{nt2}$ is 0.94 and the theoretical ratio is 0.95.

Under the condition of using FEP or PDMS as inert film, increasing tilting separation velocity causes separation force and fracture energy increase in different magnitude. When using FEP as inert film, $G_{nt}$ increases 1.48 times from 0.1mm/s to 1.5mm/s, while on PDMS film it increases 3.58 times. Tilting separation force is about 20 percent lower than pulling-up separation force when using separation velocity above 0.2mm/s, and PDMS as inert film.

The separation velocity distribution and the inert film cause the difference of stress distribution. The stress in the high velocity side of the vat is higher than the hinge side when using tilting. The structure that carrying large separation force should be put in the low stress area for avoiding defects during fabrication.

Tilting can help maintain the uniformity of material, reduce the upper platform motion for bottom-up MPSL fabrication process.

## Acknowledgements

## References

Barenblatt, G.I., 1962. The mathematical theory of equilibrium cracks in brittle fracture. Adv Appl Mech 7, 55-129.

Camanho, P.P., Davila, C., De Moura, M., 2003. Numerical simulation of mixed-mode progressive delamination in composite materials. J Compos Mater 37, 1415-1438.

Choi, J.-W., Wicker, R., Lee, S.-H., Choi, K.-H., Ha, C.-S., Chung, I., 2009. Fabrication of 3D

biocompatible/biodegradable micro-scaffolds using dynamic mask projection microstereolithography. J Mater Process Technol 209, 5494-5503.

Emami, M.M., Barazandeh, F., Yaghmaie, F., 2015. An analytical model for scanning-projection based stereolithography. J Mater Process Technol 219, 17-27.

Felzmann, R., Gruber, S., Mitteramskogler, G., Tesavibul, P., Boccaccini, A.R., Liska, R., Stampfl, J., 2012. Lithography-Based Additive Manufacturing of Cellular Ceramic Structures. Adv Eng Mater 14, 1052-1058.

Huang, Y.-M., Jiang, C.-P., 2005. On-line force monitoring of platform ascending rapid prototyping system. J Mater Process Technol 159, 257-264.

Huang, Y.-M., Lan, H.-Y., 2006. Compensation of distortion in the bottom exposure of stereolithography process. The International Journal of Advanced Manufacturing Technology 27, 1101-1112.

Hull, C.W., 1986. Apparatus for production of three-dimensional objects by stereolithography. U.S. Patent 4,575,330.

John, H., 2007. Apparatus and method for the non-destructive separation of hardened material layers from a flat construction plane. U.S. Patent 7,195,472.

Joyce, M., 2012. Solid Image Apparatus With Improved Part Separation From The Image Plate. U.S. Patent Application 13/600,729.

Kuna, M., 2013. Finite elements in fracture mechanics. Springer, New York, pp. 338-339.

Liravi, F., Das, S., Zhou, C., 2015. Separation force analysis and prediction based on cohesive element model for constrained-surface Stereolithography processes. Comput Aided Design 69, 134-142.

Pan, Y., Chen, Y., Zhou, C., 2012a. Fast recoating methods for the projection-based stereolithography process in micro-and macro-scales, Proceeding of solid freeform fabrication symposium, Austin, Texas.

Pan, Y., Zhou, C., Chen, Y., 2012b. A Fast Mask Projection Stereolithography Process for Fabricating Digital Models in Minutes. Journal of Manufacturing Science and Engineering 134, 051011.

Park, K., Paulino, G.H., 2011. Cohesive zone models: a critical review of traction-separation relationships across fracture surfaces. Applied Mechanics Reviews 64, 060802.

Renap, K., Kruth, J.P., 1995. Recoating issues in stereolithography. Rapid Prototyping Journal 1, 4-16.

Rybicki, E.F., Kanninen, M., 1977. A finite element calculation of stress intensity factors by a modified crack closure integral. Eng Fract Mech 9, 931-938.

Schwentenwein, M., Homa, J., 2015. Additive Manufacturing of Dense Alumina Ceramics. International Journal of Applied Ceramic Technology 12, 1-7.

Tumbleston, J.R., Shirvanyants, D., Ermoshkin, N., Janusziewicz, R., Johnson, A.R., Kelly, D., Chen, K., Pinschmidt, R., Rolland, J.P., Ermoshkin, A., 2015. Continuous liquid interface production of 3D objects. Science 347, 1349-1352.

Xu, K., Chen, Y., 2014. Curing Temperature Study for Curl Distortion Control and Simulation in Projection Based Stereolithography, ASME 2014 International Design Engineering Technical Conferences and Computers and Information in Engineering Conference. American Society of

Mechanical Engineers, pp. V01AT02A049-V001AT002A049.

Ye, H., Das, S., Zhou, C., 2015. Investigation of Separation Force for Bottom-Up Stereolithography Process From Mechanics Perspective, ASME 2015 International Design Engineering Technical Conferences and Computers and Information in Engineering Conference. American Society of Mechanical Engineers, pp. V01AT02A030-V001AT002A030.

Zhou, C., Chen, Y., Yang, Z., Khoshnevis, B., 2013. Digital material fabrication using mask‐image‐projection‐based stereolithography. Rapid Prototyping Journal 19, 153-165.
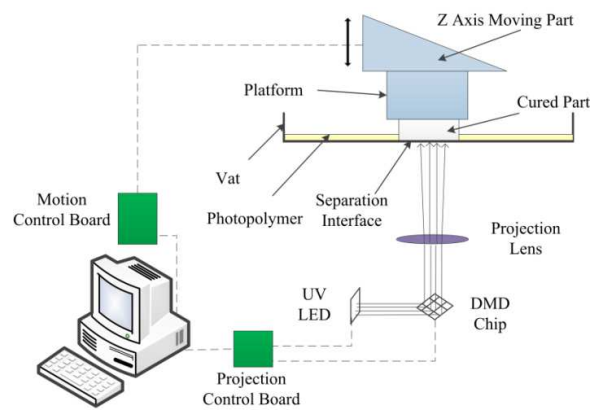
Fig. 1 Schematic of bottom-up MPSL system.

(a)



(b)
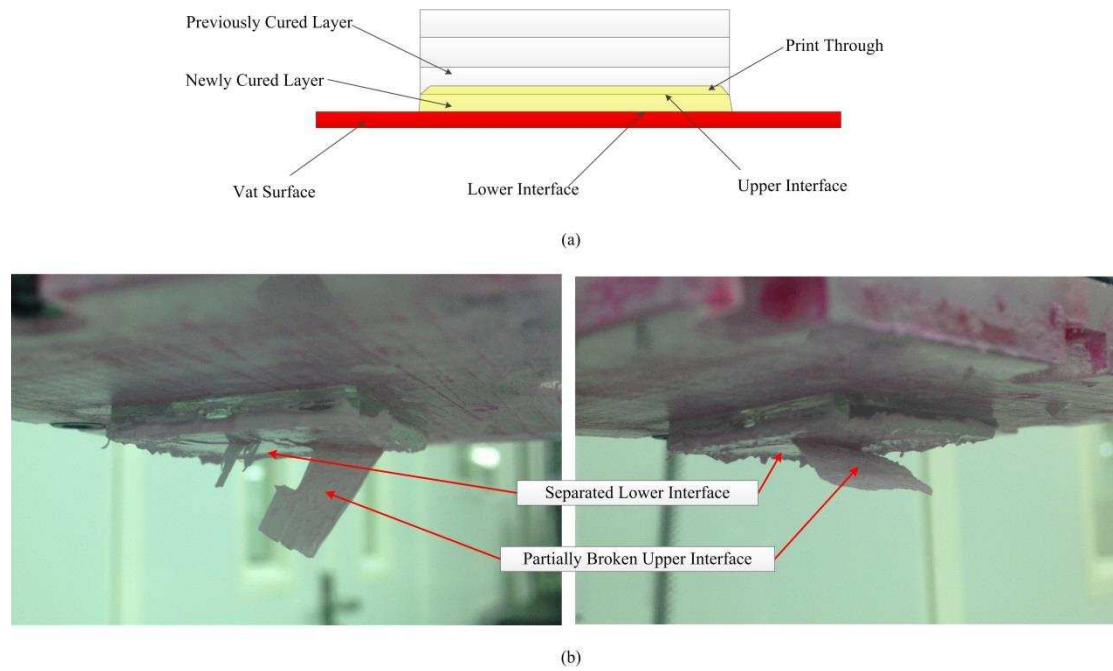
Fig. 2 (a) The formation of the upper and lower interface during each layer fabrication of bottom-up MPSL; (b) failed fabrication case that the adhesion of upper interface is weak.
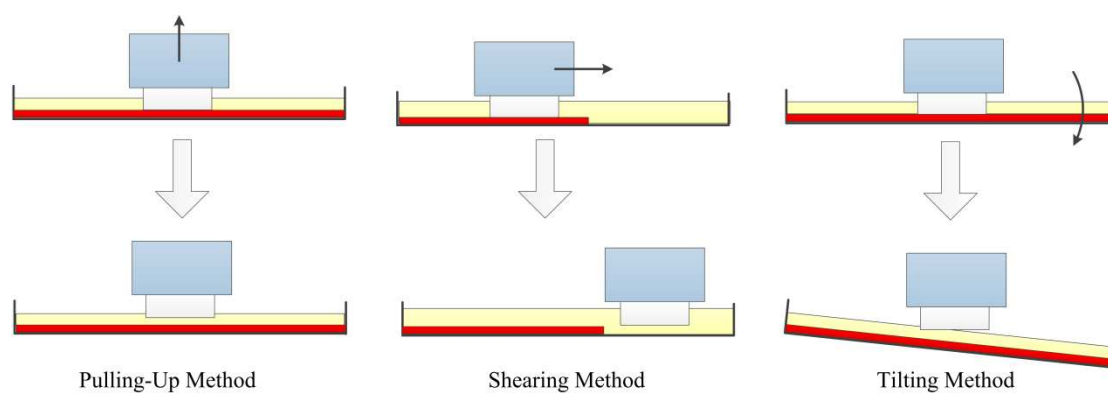
Fig. 3 Three motions of platform for separation used in both industrial and academic area.
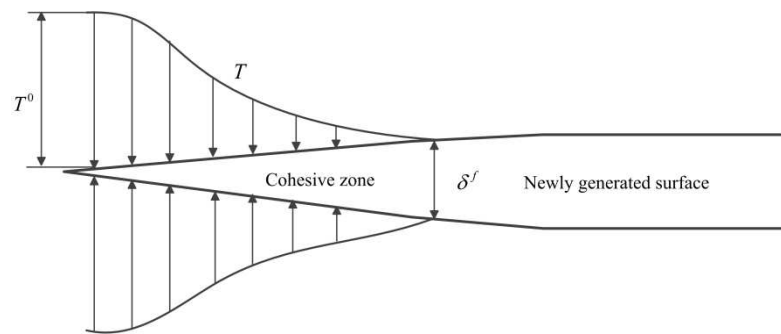
Fig. 4 The narrow strip zone assumption and the stress distribution of cohesive zone model.
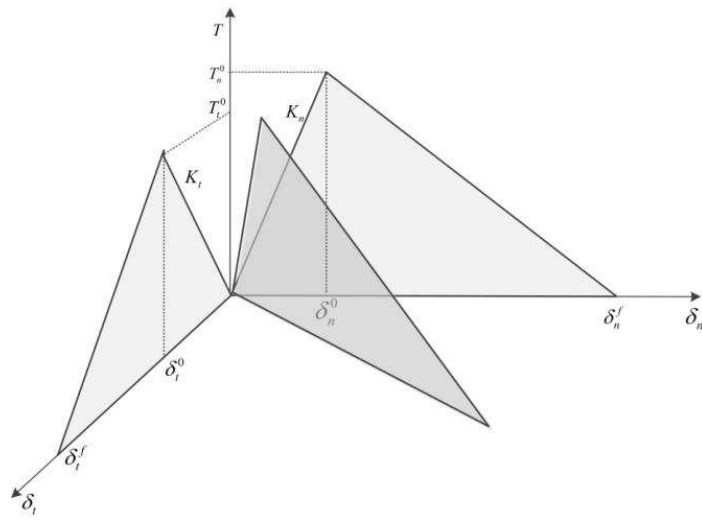
Fig. 5 The mixed-mode of bilinear cohesive law.
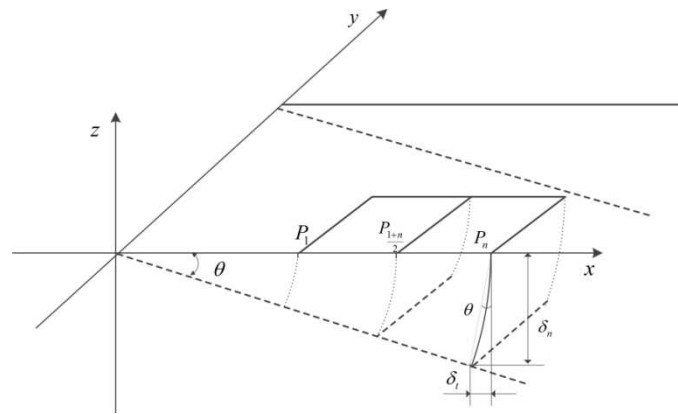
Fig. 6 Schematic of tilting separation and the normal and tangential movements between crack faces in tilting separation.
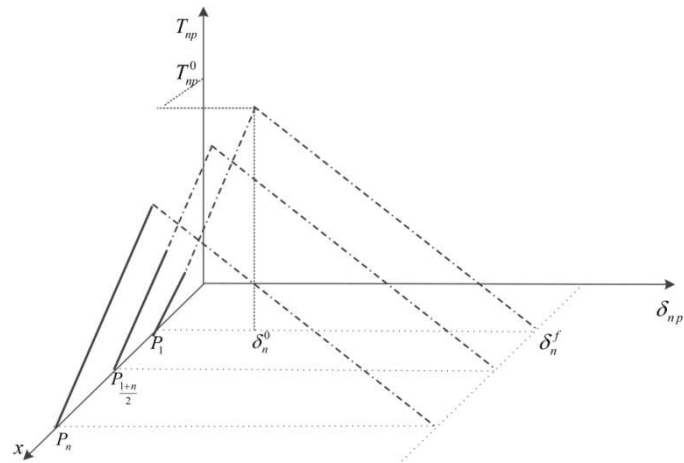
Fig. 7 The separation of each small area at the exposure area in tilting separation can be seen as pulling-up separation, and different small area around $P_i$ has its own state in the cohesive curve of pulling-up separation at the same time.
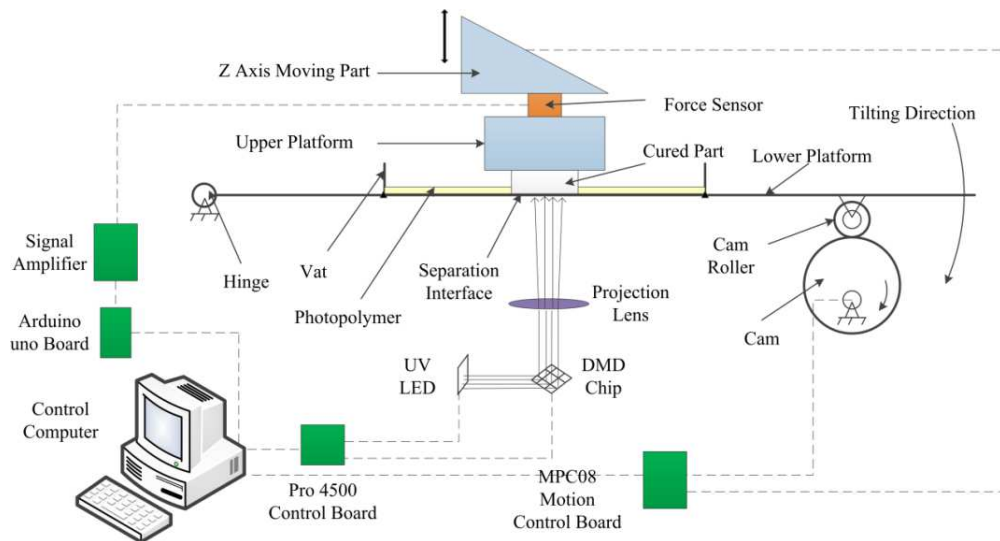
Fig. 8 Schematic of specially designed bottom-up MPSL with tilting mechanism.

1) Z Axis Moving Part
2) Force Sensor
3) Upper Platform
4) Vat
5) Lower Platform
6) Cam and Cam Rollor
7) Projection Module
8) Hinge
9) Raster Ruler
10) Voltage Signal Amplifier
11) Arduino uno Board
12) 24V Power Supply
13) Adjusting Thimbles
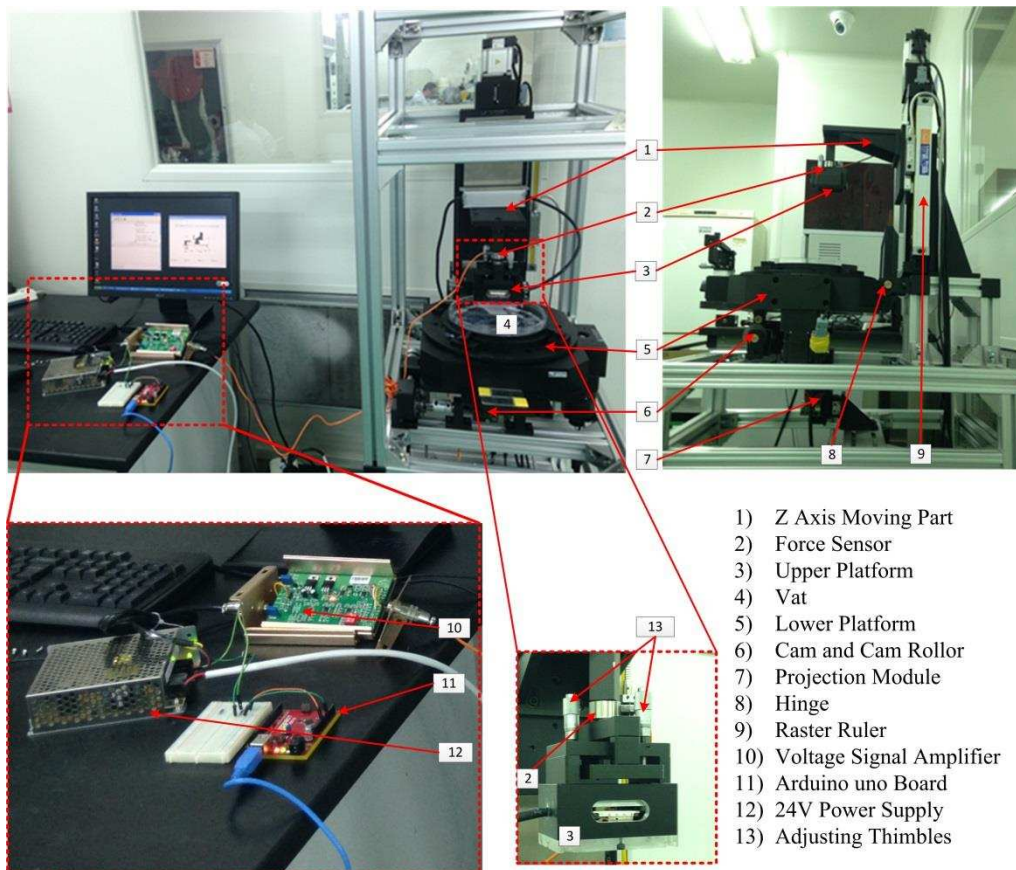
Fig. 9 Setup of the whole system and the separation force processing module.
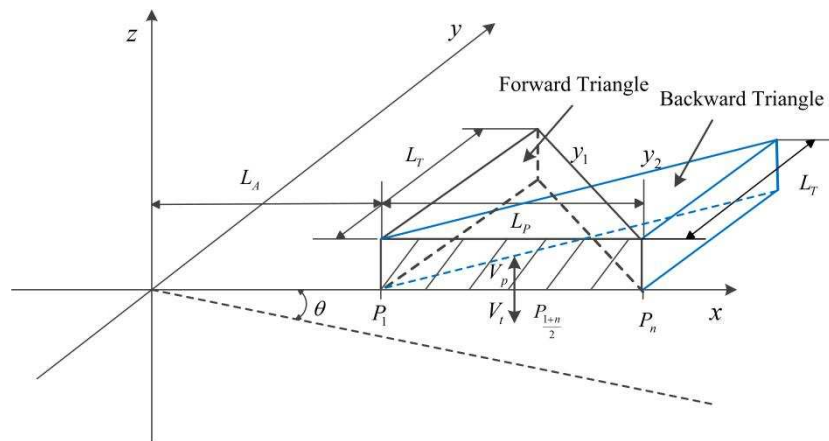
Fig. 10 Half forward and backward triangle parts are shown in different colors, and their locations and dimensions that represent the real condition of the experiment fabrication process are denoted in the three dimensional coordinate system.
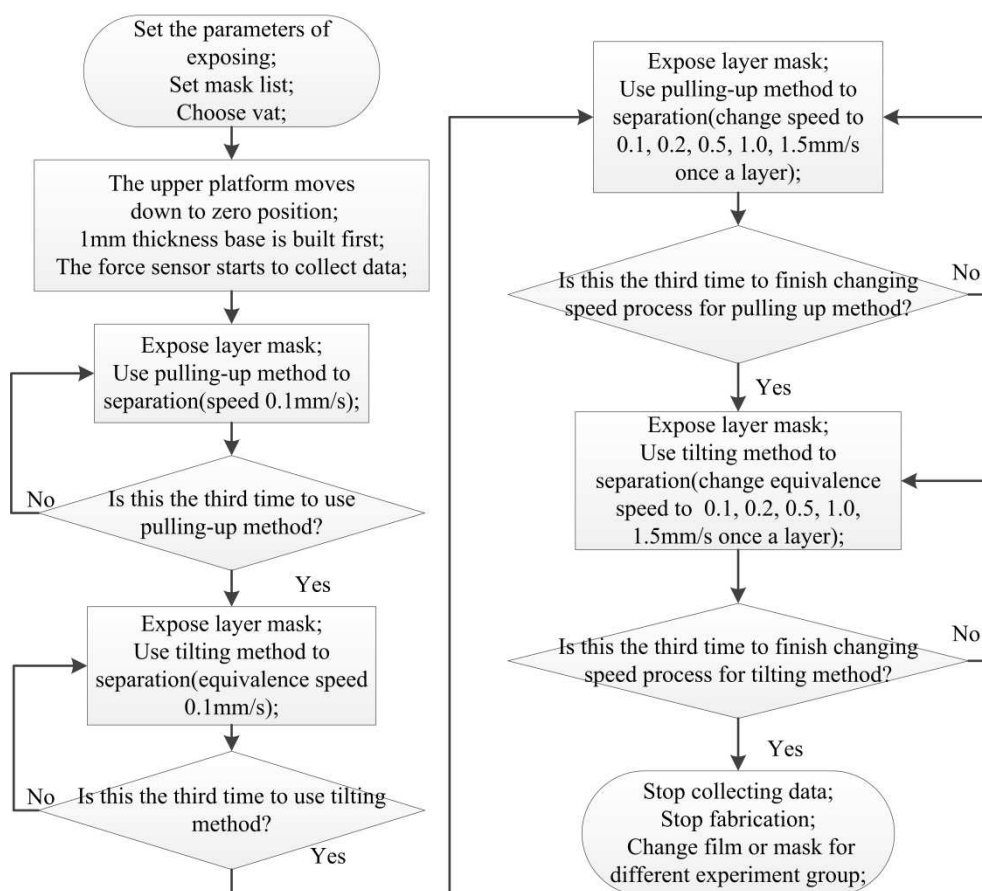
Fig. 11 Flow chart of the fabrication procedure that is used to collect separation force data automatically in order to reduce the instability of separation force.
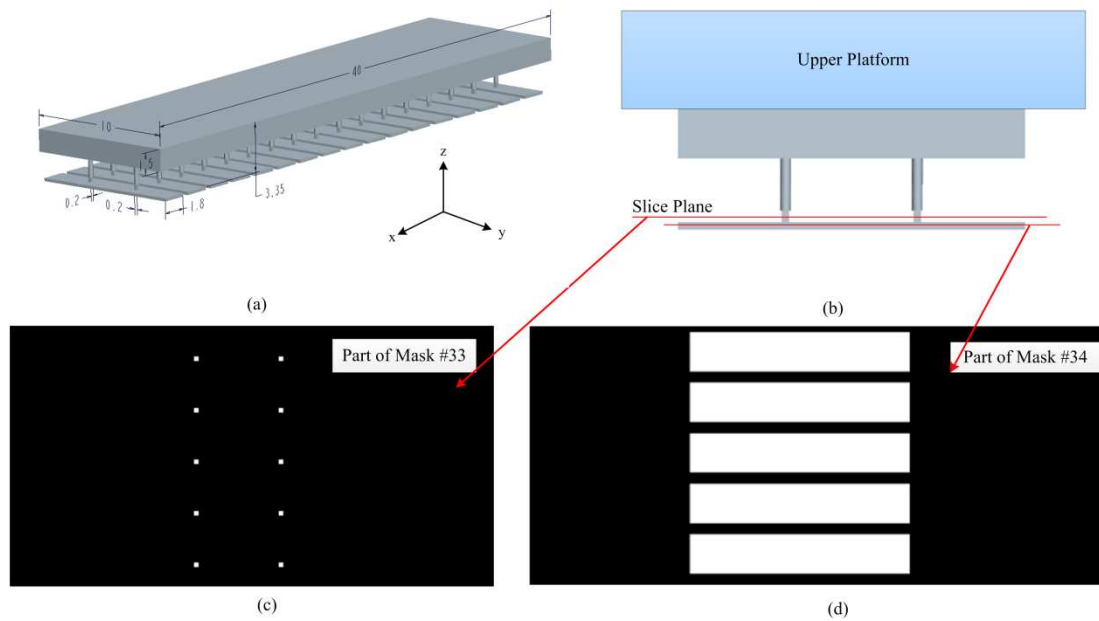
Fig. 12 The test sample and its critical masks: (a) coordination and dimension of the test sample; (b) the front view of the test sample and its build position; (c) part of the broken section mask; (d) part of the final layer rectangular mask that used to increase the separation force to break the pillars.
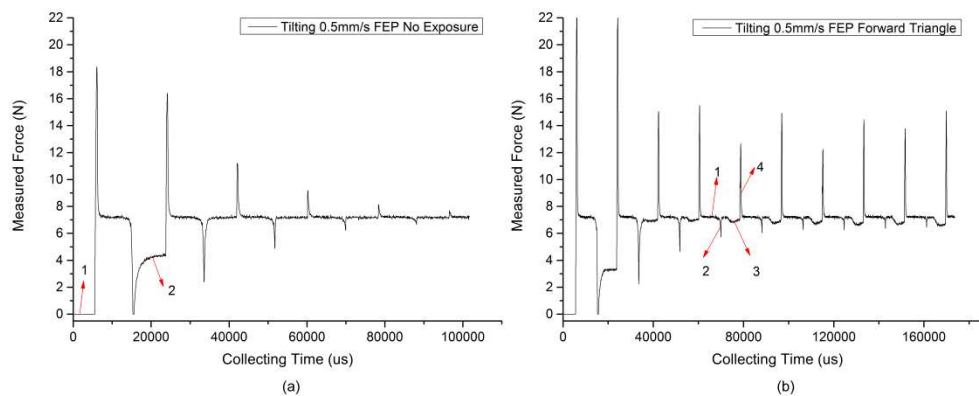
Fig. 13 The measured force from the beginning of a fabrication process (without subtraction the weight of the upper platform): (a) under the condition of no exposure (1. beginning of fabrication process after zero position registration; 2. residual force of zero registration after the reposition of the upper platform); (b) using forward triangle as mask (1. move up process of the upper platform after previous tilting separation; 2. pressure caused by the resin flow during the reposition of the lower platform; 3. exposure process; 4. tilting separation process).
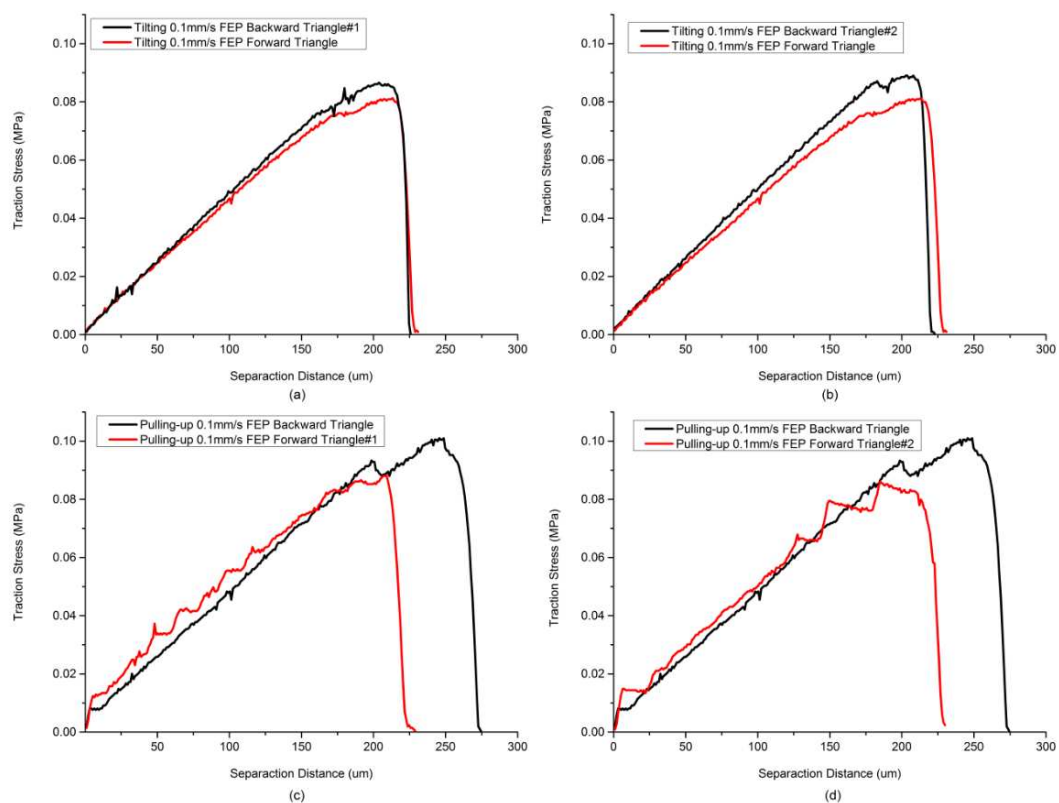
Fig. 14 The cohesive curves of tilting separation and pulling-up separation when using different orientation masks (0.1mm/s, FEP as inert film): (a) the contrast between 1-T-2#1 and 1-T-1; (b) the contrast between 1-T-2#2 and 1-T-1; (c) the contrast between 1-P-1#1 and 1-P-2; (d) the contrast between 1-P-1#1 and 1-P-2.
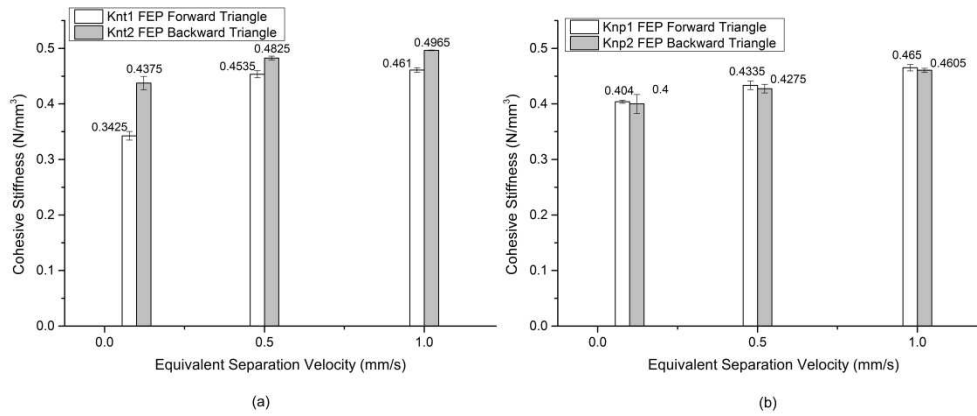
Fig. 15 The linear fit results of cohesive stiffness of tilting separation and pulling-up separation under different mask orientations (0.1mm/s, 0.5mm/s, 1.0mm/s; FEP as inert film): (a) tilting separation cohesive stiffness; (b) pulling-up separation cohesive stiffness.
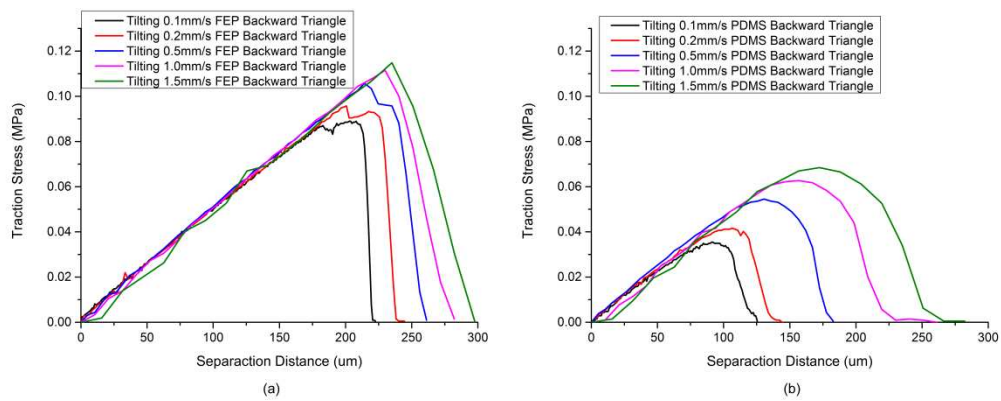
Fig. 16 The cohesive curves of tilting separation when using different separation velocities and different inert films (0.1mm/s, backward triangle): (a) the data set of 2-T-1; (b) the data set of 2-T-2.
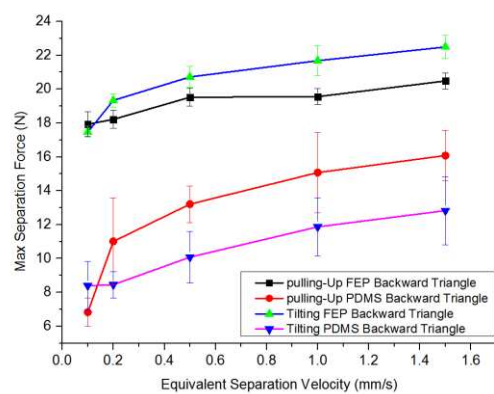
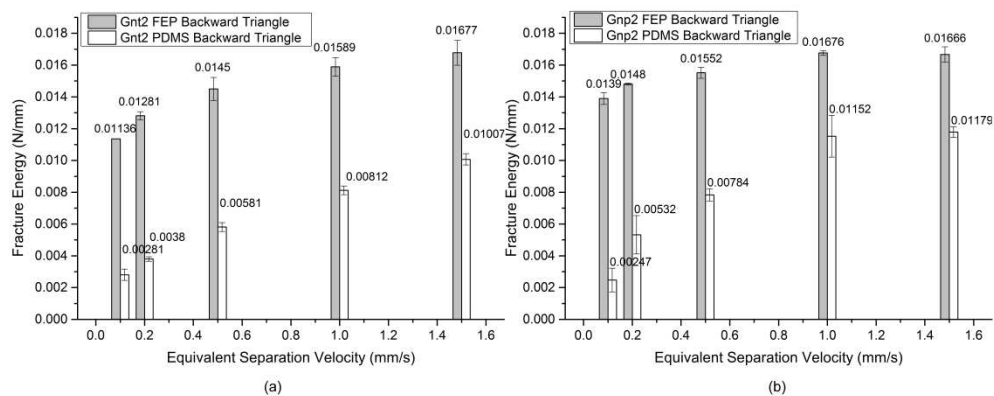Fig. 17 The maximum separation forces of data set listed in Table 5.

Fig. 18 The fracture energy of tilting separation and pulling-up separation when using different separation velocities and different inert films (calculated by integrating the cohesive curves): (a) tilting separation fracture energy under different films; (b) pulling-up separation fracture energy under different films.
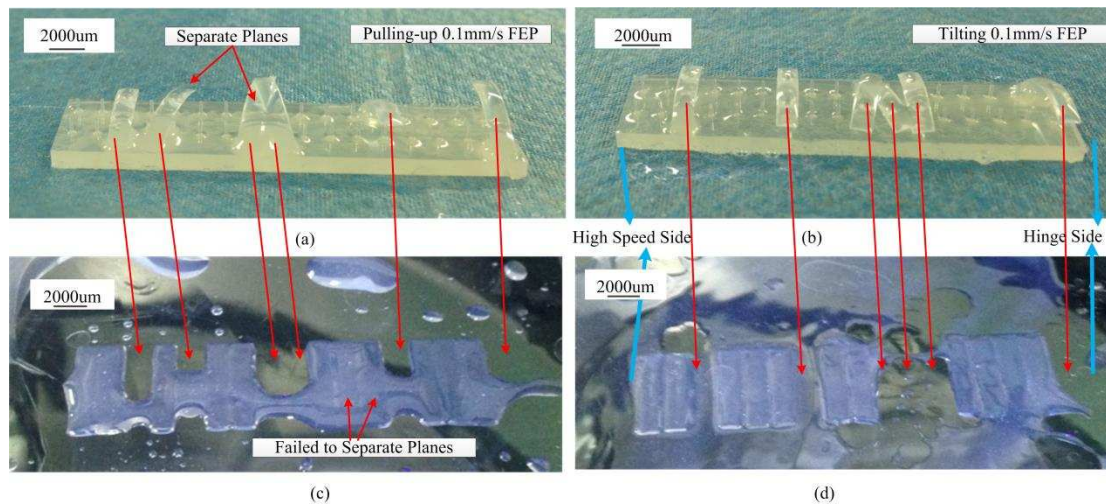
Fig. 19 Broken conditions of two test samples using pulling-up and tilting separation (0.1mm/s, FEP as inert film): (a) the test sample after final layer fabrication using pulling-up separation; (b) the test sample after final layer fabrication using tilting separation; (c) the vat surface with unseparated final layers (pulling-up); (d) the vat surface with unseparated final layers (tilting).

Fig. 20 The broken pillars cutted from the base of test sample: (a) test sample; (b) broken pillars.

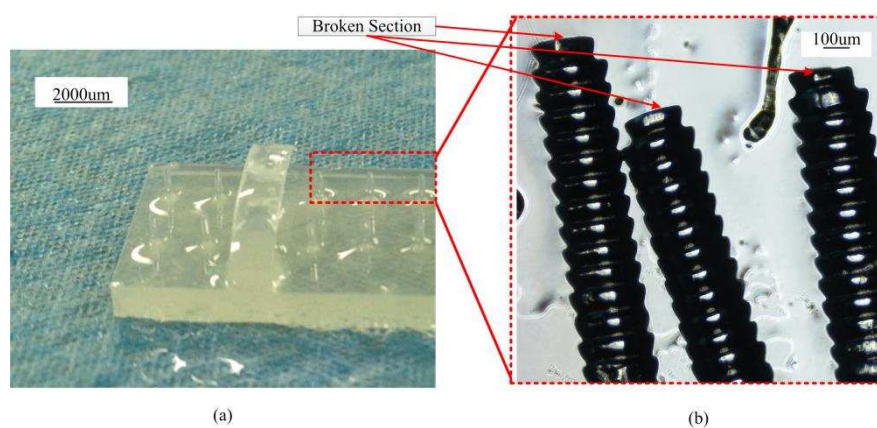Table 1 The detailed specifications and the manufacturers of the experimental setup.

| Component | Specification | Manufacturer |
|---|---|---|
| UV LED | LED area: 3.9 mm² ;Minimum power: 3W<br>Peak wavelengths: 405 nm<br>Wavelength Range: 400 - 410 nm<br>Radiometric Flux Density: 0.83 W/mm² | Luminus Devices, Inc. Billerica, MA |
| DMD™ | Micromirror dimension (Diagonal array): 0.45inch (11.43mm)<br>Micromirror tilt angle: ±12°<br>Array of aluminum micromirrors: $1140 \times 912$<br>Pitch: 7.6μm | Texas Instruments, Dallas, Texas |
| PRO 4500 Control Board | Programmable LED current<br>Video output: WXGA($1280 \times 800$) | Wintech Digital Systems Technology corp. Beijing |
| Projection Lens | Projection area: 65.6mm $\times$ 41mm<br>Projection distance: 92mm | Wintech Digital Systems Technology corp. Beijing |
| Upper platform | Accuracy of raster ruler:1μm<br>Ball screw lead: 4mm | Jiangyun Optoelectronics corp. Beijing |
| Lower platform | Radius of eccentric cam profile: 25mm<br>Radius of eccentric cam theoretical profile: 36mm<br>Eccentric distance: 9mm<br>Distance between hinge and cam roller: 275mm<br>Distance between center of upper platform and hinge: 136mm | Jiangyun Optoelectronics corp. Beijing |
| MPC08 motion control card | 4 axis stepper / servo control; Interface: PCI bus | Leetro Automation CO., LTD. Chengdu |
| Force sensor | Measuring range of force: 0-10KG<br>Sampling interval: 10.45ms<br>Range of output valtage: 0V-5V<br>Resolution of Arduino uno analog input: 10 bits | Liheng, Inc. Shanghai |
| Inert film | PDMS(1mm), FEP(0.08mm) | |
| Resin vat | Polymethyl methacrylate(PMMA, 5mm thickness) | |

Table 2 Photosensitive material and the curing parameters used in experiments.

| Photopolymer | Exposure time for each layer(s) | Light intensity (mW/cm$^2$) | Theoretical layer thickness(mm) |
|---|---|---|---|
| UV-curing Acrylic-epoxy Resin | 5 | 8.81 | 0.1 |

Table 3 The locations and dimensions of forward and backward isosceles triangle masks.

| $L_A$(mm) | $L_P$(mm) | $L_T$(mm) |
|---|---|---|
| 126 | 20 | 10 |

Table 4 The specific parameters of experiment that compared the effect of different A(x) on the cohesive stiffness of tilting separation and pulling-up separation.

| Separation data set | Separation method | Equivalent separation velocity(mm/s) | Mask | Inert film | Fabrication layers |
|---|---|---|---|---|---|
| 1-P-1 | Pulling-up | 0.1, 0.5, 1.0 | Forward triangle | FEP | 3 for each velocity |
| 1-P-2 | Pulling-up | 0.1, 0.5, 1.0 | Backward triangle | FEP | 3 for each velocity |
| 1-T-1 | Tilting | 0.1, 0.5, 1.0 | Forward triangle | FEP | 3 for each velocity |
| 1-T-2 | Tilting | 0.1, 0.5, 1.0 | Backward triangle | FEP | 3 for each velocity |

Table 5 The specific parameters of experiment that comparing the effect of different velocity on the fracture energy of tilting separation and pulling-up separation.

| Separation data set | Separation method | Equivalent separation velocity(mm/s) | Mask | Inert film | Fabrication layers |
|---|---|---|---|---|---|
| 2-P-1 | Pulling-up | 0.1, 0.2, 0.5, 1.0, 1.5 | Backward triangle | FEP | 3 for each velocity |
| 2-P-2 | Pulling-up | 0.1, 0.2, 0.5, 1.0, 1.5 | Backward triangle | PDMS | 3 for each velocity |
| 2-T-1 | Tilting | 0.1, 0.2, 0.5, 1.0, 1.5 | Backward triangle | FEP | 3 for each velocity |
| 2-T-2 | Tilting | 0.1, 0.2, 0.5, 1.0, 1.5 | Backward triangle | PDMS | 3 for each velocity |

Table 6 The comparison between theoretical ratio and experimental ratio of $K_{nt1} / K_{nt2}$ and $K_{np1} / K_{np2}$.

| | Theoretical Ratio | 0.1mm/s Ratio | 0.5mm/s Ratio | 1.0mm/s Ratio |
|---|---|---|---|---|
| $K_{nt1} / K_{nt2}$ | 0.9520 | 0.7828 | 0.9399 | 0.9285 |
| $K_{np1} / K_{np2}$ | 1.0000 | 1.0100 | 1.0140 | 1.0097 |